Spatiotemporal dynamics of voltage-induced resistance transition in the double-exchange model

Gia-Wei Chern*
Department of Physics, University of Virginia, Charlottesville, Virginia 22904, USA

(Received 28 September 2021; revised 14 December 2022; accepted 16 December 2022; published 28 December 2022)

We present multiscale dynamical simulations of voltage-induced insulator-to-metal transitions in the double-exchange model, a canonical example of itinerant magnets and correlated electron systems. By combining the nonequilibrium Green's function method with large-scale Landau-Lifshitz-Gilbert dynamics, we show that the transition from an antiferromagnetic insulator to the low-resistance state is initiated by the nucleation of a thin ferromagnetic conducting layer at the anode. The metal-insulator interface separating the two phases is then driven toward the opposite electrode by the applied voltage, giving rise to a growing metallic region. We further show that the initial transformation kinetics is well described by the Kolmogorov-Avrami-Ishibashi model with an effective spatial dimension that depends on the applied voltage. Implications of our findings for the resistive switching in colossal magnetoresistant materials are also discussed.

DOI: 10.1103/PhysRevB.106.245146

I. INTRODUCTION

Resistive switching (RS) in a capacitorlike system refers to the drastic changes in resistance induced by a moderate applied voltage or current [1–6]. The change of resistance is often nonvolatile and reversible. The RS effect is not only fascinating by itself but also has important technological implications, especially for applications in nonvolatile information storage, memristor devices, and neuromorphic computing [7–11]. The switching dynamics in real materials is a complex process which involves a large variety of microscopic mechanisms, ranging from the thermal effect [12] and ionic migration [13] to dielectric breakdown [14] and Mott transition [15]. Also, importantly, spatial inhomogeneity at the nanoscale plays a crucial role in the resistance transition dynamics. Indeed, extensive experiments have now established that the huge modification of resistance results from the geometrical transformation of metallic clusters, which could comprise only a small fraction of the driven system in some materials. Depending on the geometrical pattern of the conducting paths, the RS can be roughly classified into the filamentary and interface types.

Perhaps the most studied mechanism of RS is the ionic transport facilitated by the electrochemical redox reactions in several oxides. In such systems, the switching is controlled by the nanoscale dynamics of ion migration. During the so-called electroforming step, metallic filaments that bridge the two electrodes are formed through electrochemical reactions. The subsequent set and reset operations correspond to the dissolution and re-growth, respectively, of the filaments. These mobile ions could be oxygen vacancies already existing in the materials or cations from the metal electrodes. Theoretical modeling of nano-ionic-based RS has reached a high level of sophistication. For example, numerical simulations of the ionic filament dynamics ranging from reactive molecular dynamics [16,17], kinetic Monte Carlo [18–21], to the continuum diffusion-reaction equation [22–25] coupled with solvers for heat transport and electrostatic potential have been carried out. On even larger length scales, effective resistor network or random circuit breaker models [26,27] have been developed to study the statistical and scaling behaviors of filamentary structures [28].

RS phenomena have also been reported in correlated electron materials in which the switching mechanism is likely of electronic origin. These include the colossal magnetoresistance (CMR) manganites such as $La_{1-x}Sr_xMnO_3$ (LSMO) [29–32] and several canonical Mott insulators including vanadium oxides [15,33–36]. RS in the ternary chalcogenides is believed to be driven by Mott insulator-to-metal transition [36]. Since electron correlation in these materials can be manipulated by various external perturbations such as pressure, temperature, or magnetic field, RS based on correlated electron materials is particularly attractive for multifunctional device applications.

Contrary to the nano-ionic RS, theoretical models of resistance transition in correlated electron systems remain mostly at the phenomenological level. For example, effective resistor network models have been developed to describe the filament structure and dynamics of the switching phenomena [37,38]. While such empirical approaches capture some of the macroscopic features, they do not shed light on the crucial interplay between the microscopic electronic processes and the macroscopic transformation dynamics, hence are limited in their predictive power as quantitative tools for materials design. A comprehensive theory of RS in correlated electron systems thus requires a multiscale approach that includes the microscopic electronic calculation and the mesoscopic pattern formation simulations.

In this paper, we present a large-scale dynamical simulation of resistance transition in the double-exchange (DE) model, which is one of the representative correlated

*gchern@virginia.edu

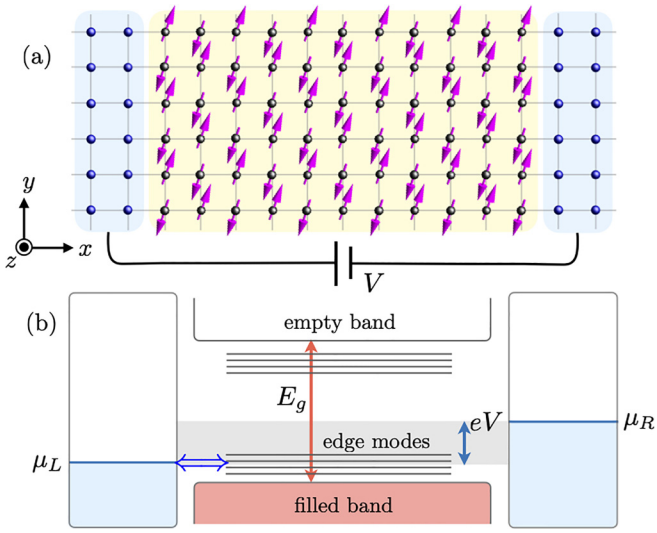

FIG. 1. (a) Schematic diagram of the voltage-driven magnetic transition in the double-exchange (DE) model sandwiched by two electrodes. In the initial state, spins in the DE model are arranged in a staggered Néel order. A voltage drop V is applied to the two electrodes. (b) Energy diagram of the system. The DE model in a Néel state is a band insulator with an energy gap $E_g = 2J_{\rm H}$. While the electron chemical potentials of both electrodes lie within the gap, a potential difference is introduced by the voltage: $\mu_{\rm R} - \mu_{\rm L} = eV$.

electron systems. The DE model describes itinerant electrons interacting with local magnetic moments [39–41]. The double exchange mechanism also plays an important role in the CMR phenomena observed in several manganites and diluted magnetic semiconductors [42,43]. Since the delocalization of charge carriers requires the alignment of electron spin with the local magnetic moment, the electronic properties of a DE system depend crucially on its magnetic state. Indeed, the competition between metallic ferromagnetic (FM) clusters and insulating antiferromagnetic (AFM) domains underlies the physics of metal-insulator (MI) transition in DE systems. Importantly, the MI transformation process is controlled by the dynamical evolution of local magnetic moments, with driving force obtained from solutions of the nonequilibrium electron subsystem. To understand this complex multiscale phenomenon, we develop a numerical framework that efficiently integrates the nonequilibrium Green's function (NEGF) method [44–48] with the Landau-Lifshitz-Gilbert (LLG) equation for the spin dynamics.

Here, we consider the voltage-induced resistance transition in a DE model sandwiched by two electrodes in a capacitor structure shown in Fig. 1(a). The DE system is initially in an insulating metastable Néel state with a large bandgap E_g determined by the electron-spin coupling constant. In the presence of an external voltage that is larger than the bandgap $eV > E_g$, charge carriers at the two electrodes could couple to electron states in the conduction and valance bands of the system. Importantly, due to the delocalized nature of these bulk states, the applied voltage immediately leads to a finite current flow. The bulk of the system quickly becomes unstable and undergoes a fast transformation to a conducting state through a process like the dielectric breakdown.

In this paper, we instead focus on an insulator-to-metal transition that is induced by a voltage smaller than the bandgap, $eV < E_g$. As shown in Fig. 1(b), the chemical potentials $\mu_{\rm L}$ and $\mu_{\rm R}$ of the two electrodes lie within the bandgap in this scenario. Due to the energy mismatch, electrons at the two electrodes cannot efficiently couple to the eigenstates in the bulk. The instability, however, starts at the left edge that is connected to the anode with a chemical potential $\mu_{\rm L}$ lower than that in the bulk (yet still higher than the valence band edge). Importantly, this coupling leads to a reduction of electron density at the left edge. As a result, antiparallel spins are unstable against the delocalization of holes through the DE mechanism. The subsequent re-alignment of spins leads to the formation of hole-rich FM clusters at the boundary.

The above scenario can also be understood from the energy diagram shown in Fig. 1(b). The coupling to the two electrodes creates a series of energy states localized at the two edges. As the applied voltage is increased, the chemical potential $\mu_{\rm L}$ of the anode is lowered toward the energy levels of the localized modes at the left edge. These edge modes are like the band-tail states introduced by disorder. The resultant resonant coupling between electrons at the left electrode and the edge modes leads to an instability toward the formation of a FM layer as electrons are drawn from the sample through the edge modes. The subsequent expansion of the FM domain drives the transformation to the metallic state. Here, we perform the NEGF-LLG simulation to provide a quantitative understanding of the above nucleation and growth scenario of insulator-to-metal phase transformation in the single-band DE model.

The rest of the paper is organized as follows. In Sec. II, we discuss the real-space NEGF-LLG method for simulating the adiabatic dynamics of driven DE systems. We next present in Sec. III the simulation results for the voltage-induced insulator-to-metal transition of a square-lattice DE model. A detailed analysis of the phase transformation kinetics and the propagation of MI interface is discussed in Sec. IV. Finally, we present a summary and outlook in Sec. V.

II. ADIABATIC SPIN DYNAMICS FOR DRIVEN DE SYSTEMS

We consider a two-dimensional (2D) capacitor structure, shown in Fig. 1(a), in which the central region is described by a square-lattice DE Hamiltonian:

$$\mathcal{H}_{\rm DE} = -t_{\rm nn} \sum_{\langle ij \rangle} \sum_{\alpha=\uparrow,\downarrow} (c^\dagger_{i,\alpha} c_{j,\alpha} + \text{H.c.}) - J_{\rm H} \sum_i \sum_{\alpha,\beta=\uparrow,\downarrow} \mathbf{S}_i \cdot c^\dagger_{i,\alpha} \boldsymbol{\sigma}_{\alpha\beta} c_{i,\beta}, \quad (1)$$

where $\langle ij \rangle$ denotes nearest neighbor pairs, $t_{\rm nn}$ is the nearest neighbor hopping constant, $J_{\rm H}$ is the onsite Hund's rule coupling constant between local spin $\mathbf{S}_i$ and conduction electron spin $\mathbf{s}_i = \sum_{\alpha,\beta} c^\dagger_{i,\alpha} \boldsymbol{\sigma}_{\alpha\beta} c_{i,\beta}$. In manganites, typical values for the hopping coefficient and Hund's rule coupling are $t = 0.5$ eV and $J_{\rm H} \sim 2$ eV, respectively [49]. The classical spins are related to the magnetic moment $\mathbf{M}_i$ of localized d electrons via $\mathbf{S}_i = \mathbf{M}_i / M_s$, where M_s is the saturation magnetization. For manganites, $M_s \sim 10^5$ A/m. This single-band DE model exhibits several features that are typical of strongly correlated electron systems, such as a

filling-controlled insulator-to-metal transition and electronic phase separation [50–53]. The DE model could thus serve as a simple prototype model system to investigate the voltage-driven MI transition in correlated electron materials. Since the DE mechanism is crucial to the CMR effect in manganites [42,43], this paper also sheds light on RS phenomena observed in lanthanum manganites such as $La_{1-x}A_xMnO_3$ (A = Ca, Sr) [29–32].

The semiclassical dynamics of local spins in the DE model is governed by the stochastic LLG equation [54,55]:

$$\frac{d\mathbf{S}_i}{dt} = \gamma \mathbf{S}_i \times (\mathbf{H}_i + \boldsymbol{\zeta}_i) - \gamma\lambda \mathbf{S}_i \times [\mathbf{S}_i \times (\mathbf{H}_i + \boldsymbol{\zeta}_i)], \quad (2)$$

where γ is a gyromagnetic ratio, λ is a dimensionless damping coefficient, $\mathbf{H}_i$ is the local exchange field, and $\boldsymbol{\zeta}_i(t)$ denotes a fluctuating field described by a Gaussian stochastic process [55]:

$$\langle \boldsymbol{\zeta}_i(t) \rangle = 0$$
$$\langle \zeta_{i,m}(t)\zeta_{j,n}(t') \rangle = \delta_{ij}\delta_{mn}\delta(t-t')\frac{2\lambda}{1+\lambda^2}\frac{k_BT}{\gamma}, \quad (3)$$

where $m, n = x, y, z$ denotes the Cartesian components of the field. With dimensionless spins $\mathbf{S}_i$, the effective field has the dimension of energy $|\mathbf{H}_i| \sim J_H$, and the gyromagnetic ratio γ has a dimension of [frequency/energy]. Importantly, the product γJ_H has the dimension of frequency, which for manganites is of the order of tens of gigahertz from microwave FM resonance measurement [56–58].

For the equilibrium electronic state, the exchange force is given by the partial derivative of a potential energy: $\mathbf{H}_i = -\partial E/\partial \mathbf{S}_i$, where $E = \langle \mathcal{H}_{DE} \rangle = \mathrm{Tr}(\rho_{eq}\ \mathcal{H}_{DE})$ is the energy of the quasi-equilibrium electron liquid [59,60]. For an out-of-equilibrium quantum state $|\Psi\rangle$, the energy E of the system is not a well-defined quantity. However, the force can still be computed using the generalized Hellmann-Feynman theorem [61–64], which for the DE model is given by

$$\mathbf{H}_i = -\left\langle \Psi \left| \frac{\partial \mathcal{H}_{DE}}{\partial \mathbf{S}_i} \right| \Psi \right\rangle = J_H\, \rho_{i\alpha,i\beta}(\{\mathbf{S}_i\})\, \boldsymbol{\sigma}_{\beta\alpha}. \quad (4)$$

Here, we have introduced the single-particle density matrix $\rho_{i\alpha,j\beta}(t) = \langle \Psi(t)|c^\dagger_{j\beta}c_{i\alpha}|\Psi(t)\rangle$. It is worth noting that this electron-induced nonequilibrium force is related to the spin-transfer torque (STT) in, e.g., s-d models, and current-induced phenomena such as tunneling magnetoresistance [65–69].

The square-lattice DE system is connected to a pair of noninteracting leads at the left and right boundaries. Periodic boundary conditions are assumed in the y direction. Moreover, a bath of noninteracting fermions is coupled to every lattice site. The total Hamiltonian of our system is $\mathcal{H} = \mathcal{H}_{DE} + \mathcal{H}_{res}$, where $\mathcal{H}_{DE}$ is the DE Hamiltonian in Eq. (1), and the second term describes the electrodes, reservoir degrees of freedom, and their coupling to the DE system:

$$\mathcal{H}_{res} = \sum_{k,\alpha,i} \varepsilon_k\, d^\dagger_{i,k,\alpha} d_{i,k,\alpha} - \sum_{i,k,\alpha} V_{k,i}(d^\dagger_{i,k,\alpha}c_{i,\alpha} + \mathrm{H.c.}). \quad (5)$$

Here, $d_{i,k,\alpha}$ represents noninteracting fermions from the bath (i inside the bulk) or the leads (for i on the two open boundaries), α is the spin index, and k is a continuous quantum number. For example, k encodes the band structure of the two leads.

After integrating out the reservoir fermions in both leads and the bath, the retarded Green's function matrix for the central region is

$$\mathbf{G}^r(\epsilon) = (\epsilon\mathbf{I} - \mathbf{H} - \boldsymbol{\Sigma}^r)^{-1}, \quad (6)$$

where $\mathbf{H}$ is the matrix representation of the DE Hamiltonian in Eq. (1) in site-spin space:

$$H_{i\alpha,j\beta} = t_{ij}\delta_{\alpha\beta} - J_H\delta_{ij}\mathbf{S}_i \cdot \boldsymbol{\sigma}_{\alpha\beta}, \quad (7)$$

and $\boldsymbol{\Sigma}^r$ are the self-energy matrix due to couplings to the two leads and the background heat bath:

$$\Sigma^r_{i\alpha,j\beta}(\epsilon) = \delta_{ij}\delta_{\alpha\beta}\sum_k \frac{|V_{i,k}|^2}{\epsilon - \epsilon_k + i0^+}. \quad (8)$$

The resultant level-broadening matrix $\boldsymbol{\Gamma} = i(\boldsymbol{\Sigma}^r - \boldsymbol{\Sigma}^a)$ is diagonal with $\Gamma_{i\alpha,i\alpha} = \pi\sum_k |V_{i,k}|^2\delta(\epsilon - \epsilon_k)$. For simplicity, we assume flat wide-band spectrum for the reservoirs, which leads to a frequency-independent broadening factor with two different values Γ_{lead} and Γ_{bath}. Next, using the Keldysh formula for the quasisteady state, the lesser Green's function is obtained from the retarded/advanced Green's functions: $\mathbf{G}^<(\epsilon) = \mathbf{G}^r(\epsilon)\boldsymbol{\Sigma}^<(\epsilon)\mathbf{G}^a(\epsilon)$, and the lesser self-energy is related to $\Sigma^{r/a}$ through the dissipation-fluctuation theorem:

$$\Sigma^<_{i\alpha,j\beta}(\epsilon) = 2i\,\delta_{ij}\delta_{\alpha\beta}\,\Gamma_i\, f_{FD}(\epsilon - \mu_i). \quad (9)$$

Here, $\Gamma_i = \Gamma_{\mathrm{lead}}$ or Γ_{bath} depending on whether site i is at the boundaries or in the bulk, and $f_{FD}(\epsilon - \mu_i) = 1/[\exp(\epsilon - \mu_i)/k_BT) + 1]$ is the Fermi-Dirac distribution. The local chemical potential $\mu_i = \mu_0$ for the bath, and $\mu_i = \mu_{L/R} = \mu_0 \mp eV/2$ for the two electrodes, with V being the applied voltage. The voltage here is assumed to be generated through, e.g., gating, instead of an external electric field. The main effect of the applied voltage V is thus to create the difference in chemical potentials of the two leads and the reservoir, which in turn drives the central DE system out of equilibrium. It is worth noting that there is no potential gradient within the DE system. The transmission current of this nonequilibrium state is

$$I = \int d\epsilon\, T(\epsilon)[f_L(\epsilon) - f_R(\epsilon)], \quad (10)$$

where $T(\epsilon) = \mathrm{Tr}(\boldsymbol{\Gamma}_R\,\mathbf{G}^r\,\boldsymbol{\Gamma}_L\,\mathbf{G}^a)$ is the transmission function, and $f_{L,R}(\epsilon) = f_{FD}(\epsilon - \mu_{L,R})$. We note that temperature affects the spin dynamics via the stochastic field $\boldsymbol{\zeta}_i(t)$ and the electronic system through the Fermi-Dirac function of the leads and bath.

The density matrix $\rho_{i\alpha,j\beta}$, which is required for the force calculation in Eq. (4) in the NEGF-LLG dynamics can now be computed from

$$\rho_{i\alpha,j\beta}(\{\mathbf{S}_i\}) = \int \frac{d\epsilon}{2\pi i} G^<_{i\alpha,j\beta}(\epsilon;\{\mathbf{S}_i\}), \quad (11)$$

for the quasisteady electron state [61–64]. Here, we have explicitly shown the dependence of both the Green's function and the density matrix on the instantaneous spin configuration $\{\mathbf{S}_i\}$. To implement the NEGF-LLG simulation, we first discretize the time evolution into many small steps Δt. For a given spin configuration $\{\mathbf{S}_i(t_n)\}$ at the nth time step, where $t_n = n\Delta t$, the NEGF method described above is employed to

compute the single-electron density matrix in Eq. (11). These are then used to derive the local effective fields $\mathbf{H}_i$ acting on individual spins in Eq. (4), and a second-order algorithm [70] is used to integrate the stochastic LLG equation and obtain the spin configuration $\{\mathbf{S}_i(t_{n+1})\}$ at the next time step.

We note in passing that, due to the expensive computational cost of NEGF calculation, to be discussed in detail below, large-scale LLG dynamics simulations of current-induced phenomena are often based on empirical formulas for STTs [71–74]. Such classical LLG approaches can routinely simulate very large systems with $N \sim 10^5$ spins. On the other hand, combining the NEGF method with LLG simulation offers a first-principles approach to the simulations of spin systems driven by either external voltages or currents. A hybrid approach to combine these two, as discussed in Refs. [67–69], consists of two steps. First, the NEGF method, sometimes combined with density functional theory, is used to compute the STT in advance. The computed STT is then incorporated into large-scale, yet classical LLG spin dynamics simulations [67–69].

Another approach is the real-time integration of NEGF and LLG, which means the electron degrees of freedom are integrated out on the fly using NEGF, as discussed above in this section. Since the NEGF calculation must be carried out at every time step of the LLG simulation, this approach is very time consuming. As a result, the real-time NEGF-LLG method was previously developed to simulate spin systems of relatively small sizes such as molecular magnets or one-dimensional (1D) spin chains [65,66,68], often with a few tens of spins.

Here, we apply the NEGF-LLG method to relatively large 2D systems with up to $N \sim 10^3$ spins to properly simulate voltage-driven domain wall propagation and nucleation in the DE model. The bottleneck of the simulations is the computationally expensive NEGF calculation, which has to be repeated at every time step. A total of 4000 to 5000 time steps are required for a complete simulation of the insulator-to-metal transition. The most time-consuming step is the calculation of the Green's function in Eq. (6), which requires the inversion of a $2N \times 2N$ matrix. The computational time of direct matrix inversion based on, e.g., Gauss-Jordan elimination increases dramatically with the system size due to their polynomial scaling $\mathcal{O}(N^\alpha)$, where the exponent α ranges from 2.373 to 3. Moreover, this matrix inversion must be carried out for $N_\epsilon = 3000$ different energies ϵ which covers the relevant bandwidth of the electronic subsystem.

To improve the efficiency, first, we note that thanks to the quasi-1D geometry, the Green's function is block-tridiagonal, where each block corresponds to one layer (line) of spins in the y direction. A divide-and-conquer algorithm with time complexity $\mathcal{O}(L_y^\alpha L_x)$ is implemented to invert such matrices [75–77]. Finally, highly parallel programming using MPI is implemented to simultaneously compute the Green's function at thousands of different energies.

III. NONEQUILIBRIUM INSULATOR-TO-METAL TRANSITION

We apply the above NEGF-LLG method to simulate the voltage-induced insulator-to-metal transition of the capacitor structure described by $\mathcal{H} = \mathcal{H}_{\rm DE} + \mathcal{H}_{\rm res}$. The following values are used for the model parameters: Hund's coupling $J_{\rm H} = 4.1$, level-broadening coefficients $\Gamma_{\rm lead} = 1$ and $\Gamma_{\rm bath} = 0.01$, temperature $k_{\rm B}T = 0.0025$; these energy parameters are expressed in terms of the hopping coefficient $t_{\rm nn}$. The ratio $J_{\rm H}/t_{\rm nn} \sim 4$ is consistent with the commonly used model parameters for manganites [49]. The dimensionless Gilbert damping coefficient $\lambda = 0.5$, and the time step $\Delta t = 0.25\,(\gamma t_{\rm nn})^{-1}$. The chemical potential of the bath is set at $\mu_0 = -3.2\,t_{\rm nn}$, and the chemical potentials at the two electrodes are $\mu_{\rm R/L} = \mu_0 \pm eV/2$. For convenience, in the following, the energy will be expressed implicitly in units of $t_{\rm nn}$, while time is measured in $(\gamma t_{\rm nn})^{-1}$.

The effective spin-spin interaction of the DE model depends on the electron filling fraction. Exactly at half-filling, a combination of strong local Hund's rule coupling and charge fluctuations leads to an effective nearest neighbor AFM interaction, thus stabilizing a Néel order [42,43,50,51]. The doped carriers, either through chemical or electrical methods, on the other hand, favor parallel spins through the DE mechanism [39–41]. The initial state of our simulations was obtained first using the equilibrium LLG dynamics simulations with half-filled electrons $\overline{n} \equiv \frac{1}{2}\sum_{i,\alpha} n_{i\alpha}/N = 0.5$ per site. As temperature $T \to 0$, this results in a Néel order $\mathbf{S}_i = S(-1)^{x_i+y_i}$ on the square lattice. For the band structure, a perfect Néel order is given by $E_\pm(\mathbf{k}) = \pm\sqrt{\epsilon_{\mathbf{k}}^2 + J_{\rm H}^2}$, where $\epsilon_{\mathbf{k}}$ is the energy dispersion of the square-lattice tight-binding Hamiltonian. Importantly, an energy gap $E_g = 2J_{\rm H}$ is opened in the spectrum [78]. At half-filling, the valance band $E_-(\mathbf{k})$ is completely filled, and the DE system is in a band-insulator state.

Next, we turn on the coupling to the bath at a negative chemical potential $0 > \mu_0 > -J_{\rm H}$, which still lies within the gap; see Fig. 1(b). This coupling can be thought of as a gating-induced doping at high temperatures. Importantly, this half-filled Néel state remains stable if μ_0 is within the bandgap and the temperature is low enough $k_{\rm B}T \ll |J_{\rm H} - \mu_0|$. This stability is confirmed by our NEGF-LLG simulations of the Néel state with a reduced chemical potential $\mu_0 = -3.2$ at $V = 0$ and $k_{\rm B}T = 0.0025$: a thin layer of slightly depleted electrons occurs at each of the two electrodes, while the bulk remains in the half-filled insulating state with almost perfect AFM spin order.

In the presence of an external voltage $V > 0$, a chemical potential difference $\Delta\mu = \mu_{\rm R} - \mu_{\rm L} = eV$ is introduced between the two electrodes. Crucially, the instability that leads to the insulator-to-metal transition is not driven by this potential difference. Since the bulk remains gapped at half-filling, the chemical potential difference $\Delta\mu < E_g$ is not large enough to induce a current flow, which could lead to an instability of the bulk through the DE mechanism. Instead, the instability comes from the enhanced coupling between the anode and the in-gap modes localized at the left edge when $\mu_{\rm L}$ significantly overlaps with the energy levels of these edge modes; see Fig. 1(b). This resonant coupling between the electrode and the edge modes leads to nucleation of seed FM clusters localized at the left boundary.

Figure 2 shows an example of the phase transformation of the driven DE system. The external voltage is turned on at time $t = 0$, giving rise to a chemical potential difference $eV = 1.0\,t_{\rm nn}$ at the two electrodes. Assuming $t_{\rm nn} \sim 0.5$ eV,

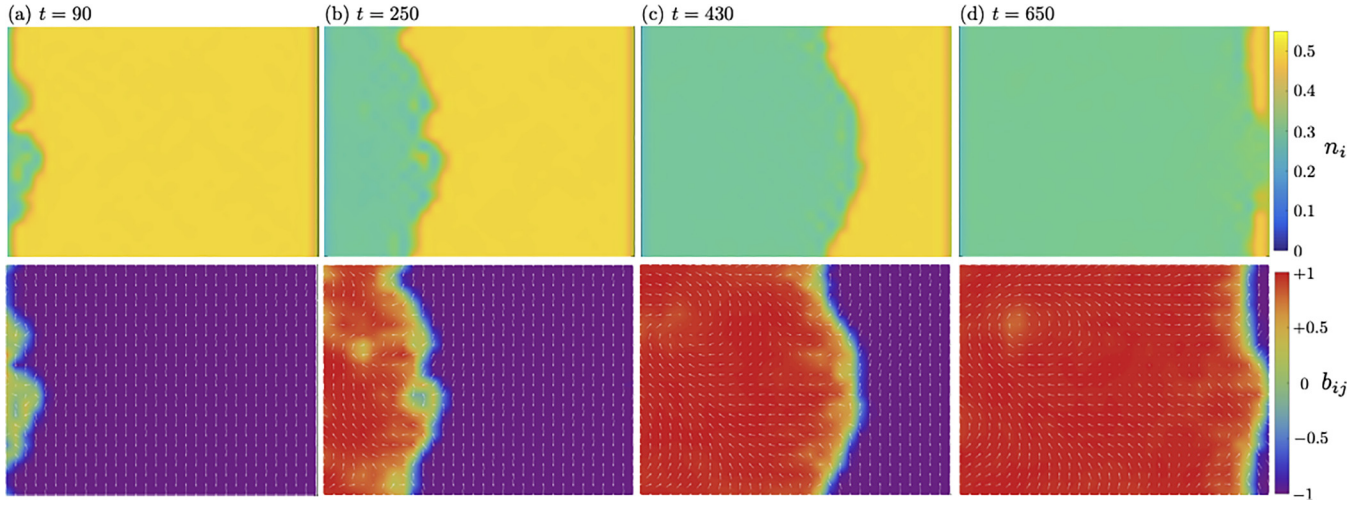

FIG. 2. Nonequilibrium Green's function (NEGF)-Landau-Lifshitz-Gilbert (LLG) simulations of a driven double-exchange (DE) model on a 32×24 square lattice. The voltage bias is applied along the longitudinal x direction. (a)–(d) Snapshots of the system at various simulation times (in units of inverse nearest neighbor hopping $t_{\rm nn}$). The top and bottom panels show the local electron density $n_i = \frac{1}{2}\sum_\alpha \langle c^\dagger_{i\alpha} c_{i\alpha}\rangle$ and the nearest neighbor spin-spin correlation $b_{ij} = \mathbf{S}_i \cdot \mathbf{S}_j$, respectively. The arrows indicate the spin orientations in the $S_x - S_z$ plane. $b_{ij} = +1$ (-1) corresponds to ferromagnetic (antiferromagnetic) bonds. Simulation parameters: Hund's coupling $J_{\rm H} = 4.1$, Gilbert damping $\alpha = 0.5$, $\Gamma_{\rm lead} = 1$, $\Gamma_{\rm bath} = 0.01$, $k_{\rm B}T = 0.0025$, time step $\Delta t = 0.25$, the average $\mu_0 = -3.2$ in the bulk. With a voltage bias $eV = 1.0$, the chemical potential at the left and right leads are $\mu_{\rm R/L} = \mu_0 \pm eV/2$.

this corresponds to an applied voltage of $V \sim 0.5$ V, consistent with the characteristic voltage for RS in manganites [30]. The top panels show the snapshots of local electron filling fraction $n_i = \frac{1}{2}\sum_\alpha \langle c^\dagger_{i\alpha} c_{i\alpha}\rangle$ at different times of the NEGF-LLG simulations, while the corresponding spin configurations are shown in the bottom panels.

As discussed above, the nonequilibrium phase transformation starts with the nucleation of the FM regions at the left edge as electrons are drained to the anode. As the nuclei merge to form a hole-rich domain, a MI interface is created and driven to the right by the voltage stress. Across the MI interface, the electron density n_i changes from $n_e \sim 0.5$ on the insulating side to $n_e \sim 0.3$ on the metallic side. To characterize the spin configurations, we introduce a nearest neighbor bond variable $b_{ij} = \mathbf{S}_i \cdot \mathbf{S}_j$, which is insensitive to the global rotations of spins. The bond variable serves as an indicator for the short-range spin correlations. As expected from the DE mechanism [50–52], FM spin correlation develops in the nucleated hole-rich regions, while the insulating domain remains dominated by AFM order; see the bottom panels in Fig. 2.

A more quantitative description of the voltage-driven phase transformation is summarized in Fig. 3, which shows the time dependence of the transmission current I, the spatially averaged electron filling fraction $\overline{n} = \frac{1}{2N}\sum_{i,\alpha}\langle c^\dagger_{i\alpha} c_{i\alpha}\rangle$, the Néel or AFM order parameter $\mathcal{N} \equiv |\frac{1}{N}\sum_i (-1)^{x_i+y_i}\mathbf{S}_i|$, and the spatially averaged bond variable $\overline{b} = \frac{1}{2N}\sum_{\langle ij\rangle} b_{ij}$. The initial nucleation of the FM clusters is characterized by an incubation timescale $t_{\rm inc}$. During this period, spins at the left edge gradually realign themselves and form seeds of hole-rich FM clusters. The AFM order parameter and the electron filling only decrease noticeably for $t \gtrsim t_{\rm inc}$.

After the incubation time, a clear MI interface is created. During the interval $t_{\rm inc} < t < t^*$, the resultant MI domain wall propagates across the bulk of the system. As shown in Figs. 3(a) and 3(b), the average electron filling fraction $\overline{n}$ decreases almost linearly with time, while the transmission current I remains nearly negligible during this period of domain wall propagation. The expansion of the metallic regions also results in a decrease of the AFM order parameter $\mathcal{N}$. The transformation from the AFM to the FM state is also described by the steady increase of the averaged bond variable $\overline{b}$ from $b_{\rm AMF} = -1$ to $b_{\rm FM} = +1$; see Figs. 3(c) and

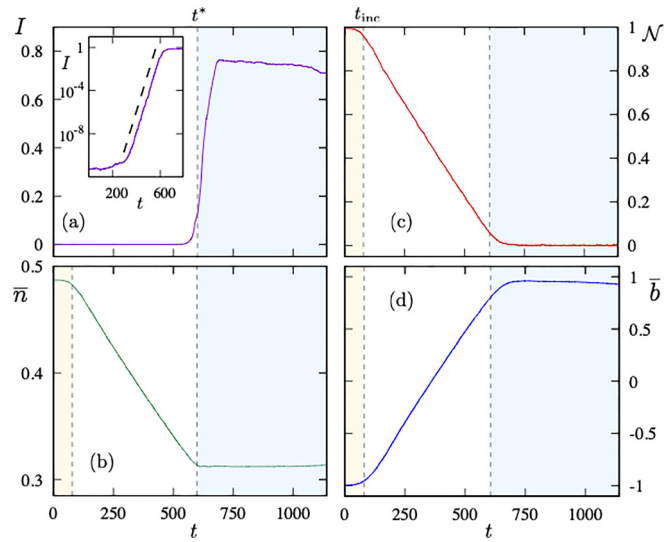

FIG. 3. Time dependence of (a) the transmission current I, (b) average electron filling fraction $\overline{n}$, (c) the antiferromagnetic order parameter $\mathcal{N}$ of spins, and (d) the average nearest neighbor spin-correlation $\overline{b} = \frac{1}{2N}\sum_{\langle ij\rangle} b_{ij}$. A constant voltage $eV = 1.0$ is applied to the double-exchange (DE) system during the interval $0 \leqslant t \leqslant t_{\rm off}$. The inset in (a) shows the exponential growth of the transmission current in a semilog plot.

3(d). As the MI interface reaches the cathode at the opposite end, the FM domain takes over the system, giving rise to a quasisteady-state regime ($t \gtrsim t^*$) characterized by a nonzero transmission current I and a low electron filling $\bar{n} \sim 0.31$.

During the propagation of the MI interface, the system remains insulating and the transmission current I is very small. Detailed examination shows that the current increases exponentially in this period. The inset of Fig. 3(a) shows the transmission current I in log scale as a function of time. The exponential growth also indicates that transmission of electrons at this stage is mainly through quantum tunneling. For an insulating AFM domain of linear size d, the tunneling current decays exponentially as the distance: $I \sim \exp(-\alpha d)$, where α is a numerical constant. Since the MI interface propagates with a roughly constant velocity, to be discussed in the following, the thickness of the AFM domain decreases linearly with time $d = L_x - vt$, leading to an exponentially increasing transmission $I \sim \exp(+\alpha v t)$.

We also compute the local density of states (DOS) from the imaginary part of the electron lesser Green's function:

$$\varrho_i(\epsilon) = \frac{1}{2\pi} \sum_{\alpha} \mathrm{Im} G^{<}_{i\alpha,i\alpha}(\epsilon). \tag{12}$$

The DOS at various layers near the anode (the left electrode with a lower chemical potential μ_L) at the beginning of the phase transition is shown in Fig. 4(a). Also shown for comparison is the bulk-averaged DOS, which exhibits a pronounced spectral gap $E_g \sim 2J_H$. In fact, the spectral gap is clearly visible even at the second layer. On the other hand, the leftmost layer ($x = 0$), which couples directly to the electrode, exhibits a broad DOS across the spectrum. This gapless DOS indicates the metallic nature of the boundary layer, where the nucleation of the hole-rich FM clusters take places.

The DOS in the quasisteady state ($t > t^*$) after the system is transformed into the FM state is shown in Fig. 4(b). One can understand these spectral functions from the band structure of an FM-ordered DE system. Here, the dispersion relation $\epsilon_{\mathbf{k}}$ of the square-lattice tight-binding model is split into two spin-polarized bands: $E_{\pm}(\mathbf{k}) = \epsilon_{\mathbf{k}} \pm J_H$, where $\pm$ refers to a band with electron spins antiparallel/parallel to the polarized local moments. A small gap $\delta = 2J_H - 8t_{nn}$ occurs at the origin when Hund's coupling is greater than half the original bandwidth. The two bands separated by a small gap at $\epsilon = 0$ in Fig. 4(b) correspond to the two spin-polarized bands of the FM state, while the two arrows indicate the position of the van Hove singularities of the original square-lattice DOS.

Figure 4(c) shows the bulk averaged DOS at different times during the phase transformation. As more and more layers become FM, the spectral gap of the AFM state is gradually filled up. The DOS is transformed into two bands with quasipolarized spins in a state with short-range FM correlation. The sharp peaks at the band edges of the AFM state also gradually evolve into two peaks originating from the van Hove singularities of spin-polarized bands of the FM state.

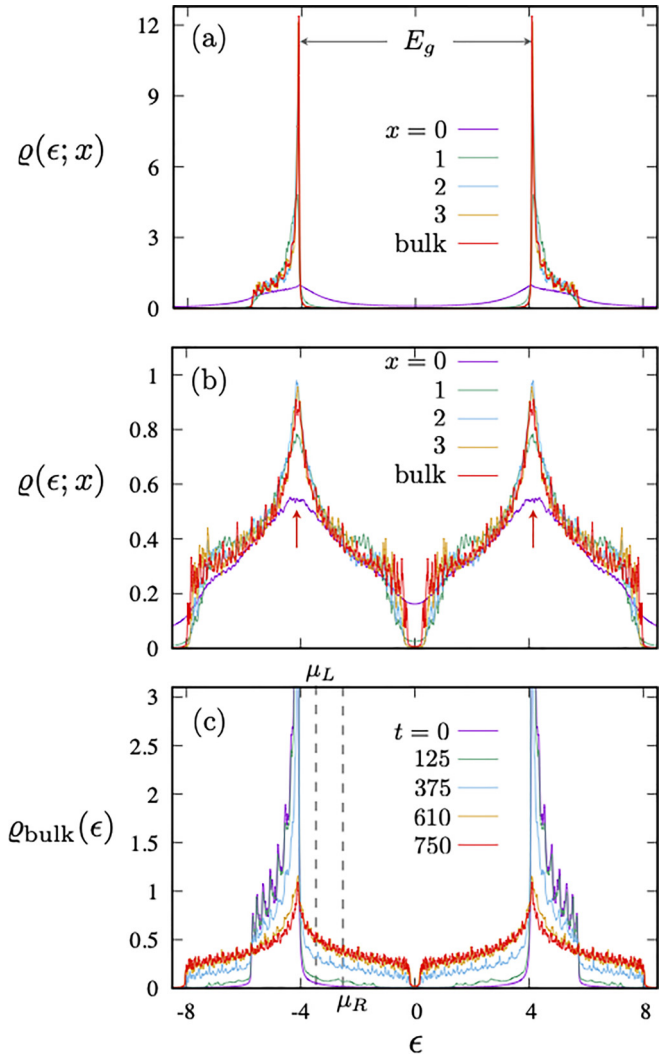

FIG. 4. (a) Local density of states (DOS) at $t = 0$, obtained from the imaginary part of the lesser Green's function (averaged over spin and the transverse y direction), for different layers x in the system. The first layer $x = 0$ couples to the left electrode. (b) Spectral function at time $t = 750$ for different layers x. In both cases, the yellow curve shows the spectral function averaged over the bulk. The two red arrows correspond to the van Hove singularities of the square-lattice DOS. (c) The bulk-averaged DOS at different times during the phase transformation. The two dashed lines indicate the position of the chemical potentials at the left and right electrodes. Hund's coupling is set at $J_H = 4.1$.

IV. KINETICS OF PHASE TRANSFORMATION

Next, we turn to the kinetics of the voltage-induced phase transformation. We first consider the propagation dynamics of the MI domain walls. To this end, we first compute the electron density profile $n_e(x)$ obtained by averaging n_i over the transverse y direction. An example of the density distribution is shown in the inset of Fig. 5(a). Importantly, the electron density exhibits a sharp discontinuity, which can be used to obtain the position x_{MI} of the MI interface. Figure 5(a) shows the (normalized) displacement $\xi = x_{MI}/L_x$ of the MI interface as a function of time for different driving voltages. Notably, a linear regime characterized by a constant velocity $\xi(t) \sim vt$ emerges after the incubation time t_{inc} that accounts for the nucleation of the FM domains and the formation of the MI interface. Since quenched disorder is not considered in this paper, the motion of the MI interface is expected to be in

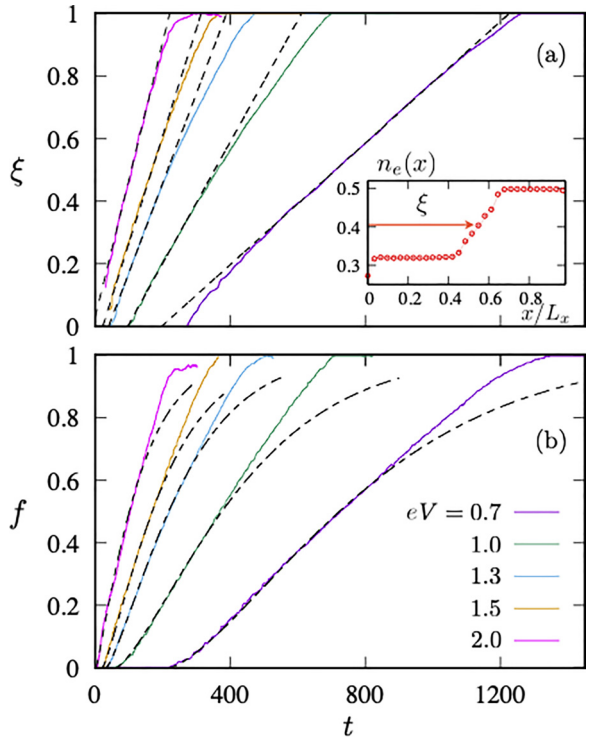

FIG. 5. (a) Displacement ξ of the metal-insulator (MI) interface as a function of time for different driving voltages. The dashed lines are fittings to linear function $\xi(t) = vt + \text{const}$. The inset shows the local electron filling $n_e(x)$ (averaged over the transverse y direction) at $t = 750$ for $eV = 0.7$. (b) Volume fraction f of the transformed ferromagnetic (FM) metallic phase vs time for varying applied voltages. Dashed lines are best fit curves using the Kolmogorov-Avrami-Ishibashi (KAI) formula in Eq. (13). The double-exchange (DE) coupling in both panels is set at $J_H = 4.1$.

the so-called flow regime [79,80] in which the velocity is proportional to the driving force, $v \sim eV$. This behavior is confirmed in our simulations except for very large applied voltage; see Fig. 6(a). In the presence of quenched disorder, the propagation of the MI interface at small voltage is expected to exhibit creep motion and depinning dynamics [79].

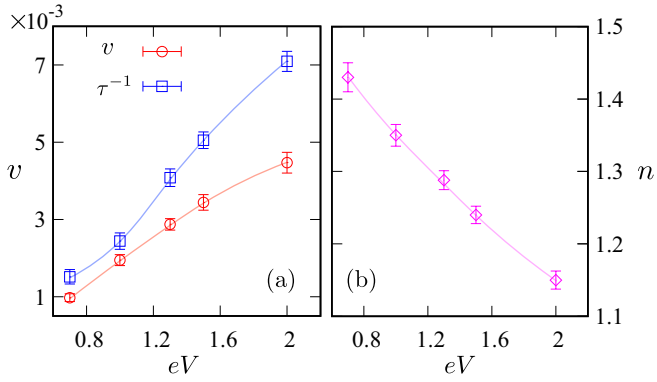

FIG. 6. (a) Velocity $v = d\xi/dt$ of the metal-insulator (MI) interface as a function of applied chemical potential difference $\Delta\mu = eV$. Also shown is the inverse characteristic time τ^{-1} as a function of eV. (b) Kolmogorov-Avrami-Ishibashi (KAI) exponent n as a function of applied voltage.

To characterize the early stage of the phase transition and particularly the nucleation of the FM domains, we compute the time-dependent volume fraction $f(t)$ of the transformed hole-rich FM phase, which is shown in Fig. 5(b) for varying voltage stresses. These curves are then fitted using the Kolmogorov-Avrami theory which offers a general phenomenological framework to model the kinetics of domain nucleation and growth [81,82]. Following the earlier works of Ishibashi and Takagi [83], the Kolmogorov-Avrami model has been widely used to analyze the domain wall dynamics of ferroelectric transistors [84–87]. In the Kolmogorov-Avrami-Ishibashi (KAI) model, the volume fraction of the transformed phase is described by

$$f(t) = 1 - \exp\left[-\left(\frac{t - t_{\text{inc}}}{\tau}\right)^n\right], \tag{13}$$

where τ is a timescale characterizing the initial domain growth, t_{inc} denotes the incubation time, and n is called the Avarami exponent. The inverse timescale τ^{-1} extracted from the fitting is shown in Fig. 6(a) as a function of voltage. As expected, the time required to grow the proto-FM domain decreases with increasing driving force.

On the other hand, useful information about the growth kinetics is encoded in the Avrami exponent. The original KAI theory predicts that the exponent $n = r + D$ [83], where D is the spatial dimension and the parameter $r = 1$ for constant nucleation rate, and $r = 0$ for preexisting nuclei. Since nucleation of the FM domain only takes place at the electrode, the Avrami exponent is expected to be given by the dimension $D = 2$ in the square-lattice DE model. Interestingly, we find that our NEGF-LLG simulation results can be well described by the KAI mechanism albeit with a noninteger Avrami exponent that decreases with increasing voltage; see Fig. 6(b). Such a fractional effective dimension indicates the nontrivial growth geometry of our system [83,88]. One can also understand the voltage dependence as follows. At large voltage stress, the uniform and roughly simultaneous nucleation at the edge of the system results in a unidirectional domain growth and an exponent $n \sim 1$. On the other hand, the sporadic and nonuniform distribution of the nucleation sites in the case of small voltages give rise to a growth kinetics that preserves some 2D nature of the system, as demonstrated in the case of Fig. 2(a).

V. CONCLUSIONS AND OUTLOOK

To summarize, we have uncovered surface-induced insulator-to-metal transformation in a DE system driven by an external voltage. The instability of the initial insulating Néel state is triggered by the coupling between the electrode and the in-gap modes that are localized at the sample boundary. Our multiscale NEGF-LLG simulations show that the phase transformation proceeds via the nucleation of a metallic layer at the anode and the subsequent propagation of the MI domain wall through the system. The initial nucleation and growth of the FM domains are well described by the KAI model with an effective dimension depending on the voltage stress. The resultant FM-AFM domain wall propagates through the system with an approximately constant velocity, which increases with the driving voltage. At the end of the phase transformation, the

driven DE system enters a nonequilibrium quasisteady state with a nonzero transmission current.

In the NEGF-LLG simulations, the thermal effects are included in the Langevin stochastic field of the LLG equation and the broadening of the Fermi-Dirac distribution of electrons at the leads and heat bath, which are kept at thermal equilibrium. In this paper, the simulations were carried out at rather low temperatures since our focus is on the interplay of the electronic driving forces and the energy dissipation during the phase transformation. Thermal fluctuations and activated dynamics are expected to play an important role at higher temperatures. Interesting topics, such as the creep motion of domain walls [79,89], will be left for future studies.

The domain wall–driven transition picture is consistent with the experiments on lanthanum manganites $La_{1-x}A_xMnO_3$ with $A =$ Sr or Ca [29–31]. A nonvolatile and bipolar switching with sharp threshold was observed in, e.g., $La_{0.8}Ca_{0.2}MnO_3$ [30]. Furthermore, using conductive atomic force microscopy, nanometer-sized conducting regions were identified during the RS. Interestingly, the size of the metallic islands was found to depend logarithmically on the pulse width of the applied electric field, a result that is consistent with the scenario of domain wall creep and depinning [90,91]. This domain wall propagation picture is further supported by the $1/f^{\alpha}$ noise of the current during RS [31], like the famous Barkhausen noise in magnetization reversal. It is worth noting that the above picture is different from the ion-migration controlled interface-type RS suggested for another manganite PCMO [13].

As the domain nucleation and expansion are mostly driven by energy exchange and dissipation, over-damped LLG dynamics with a large damping λ is used in our simulations. Indeed, overdamped LLG simulations have been widely used to study the dynamics of magnetic domain walls [92–94]. Another reason of using a large damping is due to the computational feasibility of the NEGF-LLG method. As the energy dissipation is slow with a small λ, a complete simulation of the resistance transition would take a much longer time. However, subtle effects of the precession dynamics, especially when coupled to quenched disorder, cannot be accounted for in such overdamped dynamics. Moreover, some experiments have reported a small Gilbert damping for LSMO [57], although the dissipation coefficients in manganites also depend on extrinsic factors such as temperature, thickness, and electrodes [95]. Dynamical simulations for resistance transition in DE systems with small damping and quenched disorder will be left for future work with more efficient implementation of the NEGF-LLG methods.

Another important generalization is the multiscale modeling of RS dynamics for Hubbard-type interacting models, which is relevant for RS phenomena in several canonical Mott insulators [15,33–36]. It is worth noting that complex spin-density wave patterns have been observed in the voltage-driven Hubbard model by solving the self-consistent Hartree-Fock equation with NEGF [96–98]. However, these works only consider static nonequilibrium solutions of the Hubbard model. A full dynamical modeling of RS phenomena in such systems requires further integration of NEGF-LLG with many-body techniques such as the Hartree-Fock method or dynamical mean-field theory. Surrogate many-body solver based on modern machine learning models could be a promising approach for this challenging computational task.

ACKNOWLEDGMENTS

The author thanks A. Ghosh, G. Kotliar, and Jong Han for fruitful discussions. This paper is supported by the U.S. Department of Energy Basic Energy Sciences under Contract No. DE-SC0020330. The author acknowledges Research Computing at the University of Virginia for providing computational resources and technical support that have contributed to the results reported within this paper.

[1] R. Waser and M. Aono, Nanoionics-based resistive switching memories, Nat. Mater. **6**, 833 (2007).

[2] A. Sawa, Resistive switching in transition metal oxides, Mater. Today **11**, 28 (2008).

[3] R. Waser, R. Dittmann, G. Staikov, and K. Szot, Redox-based resistive switching memories—nanoionic mechanisms, prospects, and challenges, Adv. Mater. **21**, 2632 (2009).

[4] K. M. Kim, D. S. Jeong, and C. S. Hwang, Nanofilamentary resistive switching in binary oxide system; A review on the present status and outlook, Nanotechnology **22**, 254002 (2011).

[5] D. S. Jeong, R. Thomas, R. S. Katiyar, J. F. Scott, H. Kohlstedt, A. Petraru, and C. S. Hwang, Emerging memories: Resistive switching mechanisms and current status, Rep. Prog. Phys. **75**, 076502 (2012).

[6] J. S. Lee, S. Lee, and T. W. Noh, Resistive switching phenomena: A review of statistical physics approaches, Appl. Phys. Rev. **2**, 031303 (2015).

[7] W. W. Zhuang, W. Pan, B. D. Ulrich, J. J. Lee, L. Stecker, A. Burmaster, D. R. Evans, S. T. Hsu, M. Tajiri, A. Shimaoka *et al.*, Novel colossal magnetoresistive thin film nonvolatile resistance random access memory (RRAM), in *Digest. International Electron Devices Meeting* (IEEE, San Francisco, 2002), pp. 193–196.

[8] I. G. Baek, M. S. Lee, S. Seo, M. J. Lee, D. H. Seo, D. S. Suh, J. C. Park, S. O. Park, H. S. Kim, I. K. Yoo *et al.*, *Highly scalable nonvolatile resistive memory using simple binary oxide driven by asymmetric unipolar voltage pulses*, in *IEDM Technical Digest. IEEE International Electron Devices Meeting* (IEEE, San Francisco, 2004), pp. 587–590.

[9] F. Pan, S. Gao, C. Chen, C. Song, and F. Zeng, Recent progress in resistive random access memories: Materials, switching mechanisms, and performance, Mater. Sci. Eng. R Rep. **83**, 1 (2014).

[10] M.-J. Lee, S. Seo, D.-C. Kim, S.-E. Ahn, D. H. Seo, I.-K. Yoo, I.-G. Baek, D.-S. Kim, I.-S. Byun, S.-H. Kim *et al.*, A low-temperature-grown oxide diode as a new switch element for high-density, nonvolatile memories, Adv. Mater. **19**, 73 (2007).

[11] J. del Valle, J. G. Ramirez, M. J. Rozenberg, and I. K. Schuller, Challenges in materials and devices for resistive-switching-based neuromorphic computing, J. Appl. Phys. **124**, 211101 (2018).

[12] A. A. Fursina, R. G. S. Sofin, I. V. Shvets, and D. Natelson, Origin of hysteresis in resistive switching in magnetite is Joule heating, Phys. Rev. B **79**, 245131 (2009).

[13] Y. B. Nian, J. Strozier, N. J. Wu, X. Chen, and A. Ignatiev, Evidence for an Oxygen Diffusion Model for the Electric Pulse Induced Resistance Change Effect in Transition-Metal Oxides, Phys. Rev. Lett. **98**, 146403 (2007).

[14] K. Lee, J.-S. Jang, Y. Kwon, K.-H. Lee, Y.-K. Park, and W. Y. Choi, A unified model for unipolar resistive random access memory, Appl. Phys. Lett. **100**, 083509 (2012).

[15] L. Cario, C. Vaju, B. Corraze, V. Guiot, and E. Janod, Electric-field-induced resistive switching in a family of Mott insulators: Towards a new class of RRAM memories, Adv. Mater. **22**, 5193 (2010).

[16] N. Onofrio, D. Guzman, and A. Strachan, Atomic origin of ultrafast resistance switching in nanoscale electrometallization cells, Nat. Mater. **14**, 440 (2015).

[17] T. Gergs, S. Dirkmann, and T. Mussenbrock, Integration of external electric fields in molecular dynamics simulation models for resistive switching devices, J. Appl. Phys. **123**, 245301 (2018).

[18] S. Menzel, P. Kaupmann, and W. Rainer, Understanding filamentary growth in electrochemical metallization memory cells using kinetic Monte Carlo simulations, Nanoscale **7**, 12673 (2015).

[19] S. Dirkmann, M. Ziegler, M. Hansen, H. Kohlstedt, J. Trieschmann, and T. Mussenbrock, Kinetic simulation of filament growth dynamics in memristive electrochemical metallization devices, J. Appl. Phys. **118**, 214501 (2015).

[20] S. Dirkmann and T. Mussenbrock, Resistive switching in memristive electrochemical metallization devices, AIP Adv. **7**, 065006 (2017).

[21] X. Guan, S. Yu, and H. S. P. Wong, On the switching parameter variation of metal-oxide RRAM? Part I: Physical modeling and simulation methodology, IEEE Trans. Electron Devices. **59**, 1172 (2012).

[22] S. Kim, S. J. Kim, K. M. Kim, S. R. Lee, M. Chang, E. Cho, Y. B. Kim, C. J. Kim, U. I. Chung, and I. K. Yoo, Physical electro-thermal model of resistive switching in bi-layered resistance-change memory, Sci. Rep. **3**, 1680 (2013).

[23] J. S. Lee, S. B. Lee, B. Kahng, and T. W. Noh, Two opposite hysteresis curves in semiconductors with mobile dopants, Appl. Phys. Lett. **102**, 253503 (2013).

[24] A. Marchewka, B. Roesgen, K. Skaja, H. Du, C. L. Jia, J. Mayer, V. Rana, R. Waser, and S. Menzel, Nanoionic resistive switching memories: On the physical nature of the dynamic reset process, Adv. Electron. Mater. **2**, 1500233 (2016).

[25] S. Ambrogio, B. Magyari-Köpe, N. Onofrio, M. M. Islam, D. Duncan, Y. Nishi, and A. Strachan, Modeling resistive switching materials and devices across scales, J. Electroceram. **39**, 39 (2017).

[26] S. C. Chae, J. S. Lee, S. Kim, S. B. Lee, S. H. Chang, C. Liu, B. Kahng, H. Shin, D. W. Kim, C. U. Jung *et al.*, Random circuit breaker network model for unipolar resistance switching, Adv. Mater. **20**, 1154 (2008).

[27] S. H. Chang, J. S. Lee, S. C. Chae, S. B. Lee, C. Liu, B. Kahng, D.-W. Kim, and T. W. Noh, Occurrence of Both Unipolar Memory and Threshold Resistance Switching in a NiO Film, Phys. Rev. Lett. **102**, 026801 (2009).

[28] J. S. Lee, S. B. Lee, S. H. Chang, L. G. Gao, B. S. Kang, M.-J. Lee, C. J. Kim, T. W. Noh, and B. Kahng, Scaling Theory for Unipolar Resistance Switching, Phys. Rev. Lett. **105**, 205701 (2010).

[29] X. Chen, N. Wu, J. Strozier, and A. Ignatiev, Spatially extended nature of resistive switching in perovskite oxide thin films, Appl. Phys. Lett. **89**, 063507 (2006).

[30] J.-O. Krisponeit, C. Kalkert, B. Damaschke, V. Moshnyaga, and K. Samwer, Nanoscale resistance switching in manganite thin films: Sharp voltage threshold and pulse-width dependence, Phys. Rev. B **82**, 144440 (2010).

[31] J.-O. Krisponeit, C. Kalkert, B. Damaschke, V. Moshnyaga, and K. Samwer, Time-resolved resistive switching on manganite surfaces: creep and $1/f^{\alpha}$ noise signatures indicate pinning of nanoscale domains, Phys. Rev. B **87**, 121103(R) (2013).

[32] J.-O. Krisponeit, B. Damaschke, V. Moshnyaga, and K. Samwer, Layer-by-Layer Resistive Switching: Multistate Functionality due to Electric-Field-Induced Healing of Dead Layers, Phys. Rev. Lett. **122**, 136801 (2019).

[33] C. Vaju, L. Cario, B. Corraze, E. Janod, V. Dubost, T. Cren, D. Roditchev, D. Braithwaite, O. Chauvet, Electric-pulse-driven electronic phase separation, insulator-metal transition, and possible superconductivity in a Mott insulator, Adv. Mater. **20**, 2760 (2008).

[34] E. Janod, J. Tranchant, B. Corraze, M. Querre, P. Stoliar, M. Rozenberg, T. Cren, D. Roditchev, V. T. Phuoc, M.-P. Besland *et al.*, Resistive switching in Mott insulators and correlated systems, Adv. Funct. Mater. **25**, 6287 (2015).

[35] H. Madan, M. Jerry, A. Pogrebnyakov, T. Mayer, and S. Datta, Quantitative mapping of phase coexistence in Mott-Peierls insulator during electronic and thermally driven phase transition, ACS Nano **9**, 2009 (2015).

[36] V. Dubost, T. Cren, C. Vaju, L. Cario, B. Corraze, E. Janod, F. Debontridder, and D. Roditchev, Resistive switching at the nanoscale in the Mott insulator compound $GaTa_4Se_8$, Nano Lett. **13**, 3648 (2013).

[37] T. Driscoll, J. Quinn, M. Di Ventra, D. N. Basov, G. Seo, Y.-W. Lee, H.-T. Kim, and D. R. Smith, Current oscillation in vanadium oxide: Evidence for electrically triggered percolation avalanches, Phys. Rev. B **86**, 094203 (2012).

[38] P. Stoliar, M. Rozenberg, E. Janod, B. Corraze, J. Tranchant, and L. Cario, Nonthermal and purely electronic resistive switching in a Mott memory, Phys. Rev. B **90**, 045146 (2014).

[39] C. S. Zener, Interaction between the d-shells in the transition metals. II. Ferromagnetic compounds of manganese with perovskite structure, Phys. Rev. **82**, 403 (1951).

[40] P. W. Anderson and H. Hasegawa, Considerations on double exchange, Phys. Rev. **100**, 675 (1955).

[41] P. G. de Gennes, Effects of double exchange in magnetic crystals, Phys. Rev. **118**, 141 (1960).

[42] E. Dagotto, T. Hotta, and A. Moreo, Colossal magnetoresistant materials: the key role of phase separation, Phys. Rep. **344**, 1 (2001).

[43] E. Dagotto, *Nanoscale Phase Separation and Colossal Magnetoresistance* (Springer, Berlin, 2002).

[44] Y. Meir and N. S. Wingreen, Landauer Formula for the Current through an Interacting Electron Region, Phys. Rev. Lett. **68**, 2512 (1992).

[45] A.-P. Jauho, N. S. Wingreen, and Y. Meir, Time-dependent transport in interacting and noninteracting resonant-tunneling systems, Phys. Rev. B **50**, 5528 (1994).

[46] S. Datta, *Electronic Transport in Mesoscopic Systems* (Cambridge University Press, Cambridge, 1995).

[47] H. Haug and A.-P. Jauho, *Quantum Kinetics in Transport and Optics of Semiconductors*, Springer Series in Solid-State Sciences 123 (Springer-Verlag, Berlin, 2008).

[48] M. Di Ventra, *Electrical Transport in Nanoscale Systems* (Cambridge University Press, Cambridge, 2008).

[49] See, for example, Chapter 5 for discussion of the various models for manganites and estimation of model parameters (Sec. 5.11) in Ref. [43].

[50] S. Yunoki, J. Hu, A. L. Malvezzi, A. Moreo, N. Furukawa, and E. Dagotto, Phase Separation in Electronic Models for Manganites, Phys. Rev. Lett. **80**, 845 (1998).

[51] E. Dagotto, S. Yunoki, A. L. Malvezzi, A. Moreo, J. Hu, S. Capponi, D. Poilblanc, and N. Furukawa, Ferromagnetic Kondo model for manganites: Phase diagram, charge segregation, and influence of quantum localized spins, Phys. Rev. B **58**, 6414 (1998).

[52] A. Chattopadhyay, A. J. Millis, and S. Das Sarma, $T = 0$ phase diagram of the double-exchange model, Phys. Rev. B **64**, 012416 (2001).

[53] J. Luo and G.-W. Chern, Dynamics of electronically phase-separated states in the double exchange model, Phys. Rev. B **103**, 115137 (2021).

[54] W. F. Brown, Thermal fluctuations of a single-domain particle, Phys. Rev. **130**, 1677 (1963).

[55] J. L. García-Palacios and F. J. Lázaro, Langevin-dynamics study of the dynamical properties of small magnetic particles, Phys. Rev. B **58**, 14937 (1998).

[56] G. Y. Luo, M. Belmeguenai, Y. Roussigné, C. R. Chang, J. G. Lin, and S. M. Chérif, Enhanced magnetic damping in $La_{0.7}Sr_{0.3}MnO_3$ capped by normal metal layer, AIP Adv. **5**, 097148 (2015).

[57] H. K. Lee, I. Barsukov, A. G. Swartz, B. Kim, L. Yang, H. Y. Hwang, and I. N. Krivorotov, Magnetic anisotropy, damping, and interfacial spin transport in Pt/LSMO bilayers, AIP Adv. **6**, 055212 (2016).

[58] Q. Qin, S. He, W. Song, P. Yang, Q. Wu, Y. P. Feng, and J. Chen, Ultra-low magnetic damping of perovskite $La_{0.7}Sr_{0.3}MnO_3$ thin films, Appl. Phys. Lett. **110**, 112401 (2017).

[59] V. P. Antropov, S. V. Tretyakov, and B. N. Harmon, Spin dynamics in magnets: Quantum effects and numerical simulations, J. Appl. Phys. **81**, 3961 (1997).

[60] P.-W. Ma and S. L. Dudarev, Langevin spin dynamics, Phys. Rev. B **83**, 134418 (2011).

[61] M. Di Ventra and S. T. Pantelides, Hellmann-Feynman theorem and the definition of forces in quantum time-dependent and transport problems, Phys. Rev. B **61**, 16207 (2000).

[62] T. N. Todorov, Time-dependent tight-binding, J. Phys.: Condens. Matter **13**, 10125 (2001).

[63] M. Stamenova, S. Sanvito, and T. N. Todorov, Current-driven magnetic rearrangement in spin-polarized point contacts, Phys. Rev. B **72**, 134407 (2005).

[64] J.-I. Ohe and B. Kramer, Dynamics of a Domain Wall and Spin-Wave Excitations Driven by a Mesoscopic Current, Phys. Rev. Lett. **96**, 027204 (2006).

[65] S. Salahuddin and S. Datta, Self-consistent simulation of quantum transport and magnetization dynamics in spin-torque based devices, Appl. Phys. Lett. **89**, 153504 (2006).

[66] M. D. Petrović, B. S. Popescu, U. Bajpai, P. Plechac, and B. K. Nikolić, Spin and Charge Pumping by a Steady or Pulse-Current-Driven Magnetic Domain Wall: A Self-Consistent Multiscale Time-Dependent Quantum-Classical Hybrid Approach, Phys. Rev. Appl. **10**, 054038 (2018).

[67] M. O. A. Ellis, M. Stamenova, and S. Sanvito, Multiscale modeling of current-induced switching in magnetic tunnel junctions using *ab initio* spin-transfer torques, Phys. Rev. B **96**, 224410 (2017).

[68] Y. Xie, J. Ma, S. Ganguly, and A. W. Ghosh, From materials to systems: A multiscale analysis of nanomagnetic switching, J. Comput. Electron. **16**, 1201 (2017).

[69] K. Dolui, M. D. Petrović, K. Zollner, P. Plechác, J. Fabian, and B. K. Nikolić, Proximity spin-orbit torque on a two-dimensional magnet within van der Walls heterostructure: current-driven antiferromagnet-to-ferromagnet reversible nonequilibrium phase transition in bilayer CrI_3, Nano Lett. **20**, 2288 (2020).

[70] J. H. Mentink, M. V. Tretyakov, A. Fasolino, M. I. Katsnelson, and T. Rasing, Stable and fast semi-implicit integration of the stochastic Landau-Lifshitz equation, J. Phys.: Condens. Matter **22**, 176001 (2010).

[71] J. C. Slonczewski, Current-driven excitation of magnetic multilayers, J. Magn. Magn. Mater. **159**, L1 (1996).

[72] L. Berger, Emission of spin waves by a magnetic multilayer traversed by a current, Phys. Rev. B **54**, 9353 (1996).

[73] S. Zhang and Z. Li, Roles of Nonequilibrium Conduction Electrons on the Magnetization Dynamics of Ferromagnets, Phys. Rev. Lett. **93**, 127204 (2004).

[74] D. C. Ralph, M. D. Stiles, Spin transfer torques, J. Magn. Magn. Mater. **320**, 1190 (2008).

[75] O. Hod, J. E. Peralta, and G. E. Scuseria, First-principles electronic transport calculations in finite elongated systems: A divide and conquer approach, J. Chem. Phys. **125**, 114704 (2006).

[76] M. G. Reuter, T. Seideman, and M. A. Ratner, Probing the surface-to-bulk transition: A closed-form constant-scaling algorithm for computing subsurface Green functions, Phys. Rev. B **83**, 085412 (2011).

[77] M. G. Reuter and J. C. Hill, An efficient, block-by-block algorithm for inverting a block tridiagonal, nearly block Toeplitz matrix, Comput. Sci. Disc. **5**, 014009 (2012).

[78] See, e.g., Sec. 7.6 in P. Fazekas, *Lecture Notes on Electron Correlation and Magnetism* (World Scientific, Singapore, 1999).

[79] E. E. Ferrero, L. Foini, T. Giamarchi, A. B. Kolton, and A. Rosso, Creep motion of elastic interfaces driven in a disordered landscape, Annu. Rev. Condens. Matter Phys. **12**, 111 (2021).

[80] J. Y. Jo, S. M. Yang, T. H. Kim, H. N. Lee, J.-G. Yoon, S. Park, Y. Jo, M. H. Jung, and T. W. Noh, Nonlinear Dynamics of Domain-Wall Propagation in Epitaxial Ferroelectric Thin Films, Phys. Rev. Lett. **102**, 045701 (2009).

[81] A. N. Kolmogorov, On the statistical theory of crystallization of metals, Izv. Akad. Nauk SSSR, Ser. Mat. **3**, 355 (1937) [In Russian].

[82] M. Avrami, Kinetics of phase change. I General Theory, J. Chem. Phys. **7**, 1103 (1939); II Transformation-time relations for random distribution of nuclei, **8**, 212 (1940).

[83] Y. Ishibashi and Y. Takagi, Note on ferroelectric domain switching, J. Phys. Soc. Jpn. **31**, 506 (1971).

[84] Y. W. So, D. J. Kim, T. W. Noh, J.-G. Yoon, and T. K. Song, Polarization switching kinetics of epitaxial Pb $(Zr_{0.4}Ti_{0.6})O_3$ thin films, Appl. Phys. Lett. **86**, 092905 (2005).

[85] A. Gruverman, B. J. Rodriguez, C. Dehoff, J. D. Waldrep, A. I. Kingon, R. J. Nemanich, and J. S. Cross, Direct studies of domain switching dynamics in thin film ferroelectric capacitors, Appl. Phys. Lett. **87**, 082902 (2005).

[86] P. Sharma, R. G. P. McQuaid, L. J. McGilly, J. M. Gregg, and A. Gruverman, Nanoscale dynamics of superdomain boundaries in single-crystal $BaTiO_3$ lamellae, Adv. Mater. **25**, 1323 (2013).

[87] Y. J. Kim, H. W. Park, S. D. Hyun, H. J. Kim, K. D. Kim, Y. H. Lee, T. Moon, Y. B. Lee, M. H. Park, and C. S. Hwang, Voltage drop in a ferroelectric single layer capacitor by retarded domain nucleation, Nano Lett. **17**, 7796 (2017).

[88] V. Shur, E. Rumyantsev, and S. Makarov, Kinetics of phase transformations in real finite systems: Application to switching in ferroelectrics, J. Appl. Phys. **84**, 445 (1998).

[89] L. San Emeterio Alvarez, K.-Y. Wang, S. Lepadatu, S. Landi, S. J. Bending, and C. H. Marrows, Spin-Transfer-Torque-Assisted Domain-Wall Creep in a Co/Pt Multilayer Wire, Phys. Rev. Lett. **104**, 137205 (2010).

[90] S. Lemerle, J. Ferré, C. Chappert, V. Mathet, T. Giamarchi, and P. Le Doussal, Domain Wall Creep in an Ising Ultrathin Magnetic Film, Phys. Rev. Lett. **80**, 849 (1998).

[91] P. Chauve, T. Giamarchi, and P. Le Doussal, Creep and depinning in disordered media, Phys. Rev. B **62**, 6241 (2000).

[92] J. Shao, H. Liu, K. Zhang, Y. Yu, W. Yu, H. Lin, J. Niu, K. Du, Y. Kou, W. Wei *et al.*, Emerging single-phase state in small manganite nanodisks, Proc. Natl. Acad. Sci. USA **113**, 9228 (2016).

[93] R. Wieser, Comparison of Quantum and Classical Relaxation in Spin Dynamics, Phys. Rev. Lett. **110**, 147201 (2013).

[94] C. B. Muratov, V. V. Slastikov, A. G. Kolesnikov, and O. A. Tretiakov, Theory of the Dzyaloshinskii domain-wall tilt in ferromagnetic nanostrips, Phys. Rev. B **96**, 134417 (2017).

[95] V. Flovik, F. Maciá, S. Lendínez, J. M. Hernández, I. Hallsteinsen, T. Tybell, and E. Wahlström, Thickness and temperature dependence of the magnetodynamic damping of pulsed laser deposited $La_{0.7}Sr_{0.3}MnO_3$ on (111)-oriented $SrTiO_3$, J. Magn. Magn. Mater. **420**, 280 (2016).

[96] P. Ribeiro, A. E. Antipov, and A. N. Rubtsov, Nonequilibrium breakdown of a correlated insulator through pattern formation, Phys. Rev. B **93**, 144305 (2016).

[97] J. Li, C. Aron, G. Kotliar, and J. E. Han, Microscopic theory of resistive switching in ordered insulators: Electronic versus thermal mechanisms, Nano Lett. **17**, 2994 (2017).

[98] A. Dutta and P. Majumdar, Spatial behavior in a Mott insulator near the voltage-driven resistive transition, Phys. Rev. B **101**, 245155 (2020).